

A Predictive Surrogate Model for Heat Transfer of an Impinging Jet on a Concave Surface

Sajad Salavatidezfouli¹, Saeid Rakhsha², Armin Sheidani¹, Giovanni Stabile³, and Gianluigi Rozza¹

¹Mathematics Area, MathLab, International School for Advanced Studies (SISSA), Trieste, Italy

²Department of Mechanical Engineering, Semnan University, Semnan, Iran

³Department of Pure and Applied Sciences, Informatics and Mathematics Section, University of Urbino Carlo Bo, Urbino, Italy

Abstract

This paper aims to comprehensively investigate the efficacy of various Model Order Reduction (MOR) and deep learning techniques in predicting heat transfer in a pulsed jet impinging on a concave surface. Expanding on the previous experimental and numerical research involving pulsed circular jets [1], this investigation extends to evaluate Predictive Surrogate Models (PSM) for heat transfer across various jet characteristics. To this end, this work introduces two predictive approaches, one employing a Fast Fourier Transformation augmented Artificial Neural Network (FFT-ANN) for predicting the average Nusselt number under constant-frequency scenarios. Moreover, the investigation introduces the Proper Orthogonal Decomposition and Long Short-Term Memory (POD-LSTM) approach for random-frequency impingement jets. The POD-LSTM method proves to be a robust solution for predicting the local heat transfer rate under random-frequency impingement scenarios, capturing both the trend and value of temporal modes. The comparison of these approaches highlights the versatility and efficacy of advanced machine learning techniques in modelling complex heat transfer phenomena.

Keywords: Predictive Surrogate Model; Model Order Reduction; Machine Learning; Impinging Jet; Concave Surface

1 Introduction

Owing to their high thermal efficiencies, impinging jets encompass a wide range of industrial applications including cooling of turbine blades, electronic devices, combustors walls, heat exchangers and so on [2–6]. Considering the applications which are inherently associated with a high level of oscillation like the gas turbine blades, cardinal importance is placed on the numerical and experimental study of pulsating impinging jets which has attracted a great deal of attention in recent years [7–11]. It should be noted that one of the main objectives of studying the complicated physics of such jets is to devise a way to improve cooling efficiency. In this regard, the most common strategies to reach this goal have been inlet perturbation, jet pulsation, utilization of the rough surface, and change of the nozzle geometry. [1, 12–17].

The improvement strategies can be generally divided into active/passive methods. For instance, alterations to parameters such as the nozzle diameter or the distance from the surface could be regarded as examples of passive methods, while techniques dealing with the velocity or the frequency of the impinging jet are considered as an active strategy. Therefore, in order to improve the heat transfer for an impingement jet, all the aforementioned parameters might be taken into consideration [18–22].

To illustrate, [23] in a numerical and experimental study proposed a correlation describing the relation between the Nusselt and the Reynolds number with the distance between the nozzle and the surface. As for the importance of the nozzle geometry, [24] showed that the utilization of el-

liptical jets results in a higher thermal efficiency compared to their circular counterparts. In this regard, [25] reported that the increment in the nozzle aspect ratio is directly proportional to the growth in the average Nu number on a flat plate. Owing to the importance of this issue, the investigation of the effect of the nozzle design parameters on the heat transfer of impinging jets has continued in recent years. To illustrate, [26] investigated the influence of swirl and Re number along with the distance of a nozzle on the heat transfer. The results showed that the nozzle distance significantly affects the heat transfer and as a result, it was suggested to utilize the jet at a close distance along with swirl addition for higher thermal efficiency. [27], in a numerical study, drew a comparison between the oscillating (sweeping) and constant jets for cooling the blade of a gas turbine. The results proved that the employment of sweeping jets leads to a considerable improvement in heat transfer. [28] in an experimental study, compared the flow characteristics and heat transfer of an oscillating and steady jet in a cross flow. It was reported that the heat transfer is mainly affected by the cross-flow in the case of the oscillating jet causing the alteration of the Blowing Ratio (BR), while as for the constant jets the rise in BR results in a significant increase in the heat transfer. [29] conducted a numerical and experimental study on the effect of various jet parameters, including the jet shape, on heat transfer. The upshot of their findings was that circular jets outperformed fan jets due to their higher heat transfer coefficient.

Due to the complexities associated with the physics of heat transfer in industrial applications, Machine Learn-

ing (ML) techniques have been employed to facilitate the understanding of such phenomena in recent years [30–33]. To illustrate, [34] implemented various ML techniques including k-nearest neighbour (k-NN), Random Forest (RF) and Multi-Layer Perceptron (MLP) to assess their performance regarding the numerical simulation of nano-fluid heat transfer in a micro-channel equipped with double synthetic jets. The results revealed that the k-NN algorithm yields more accurate predictions compared to the other methods employed. It should be noted that in the work of [35] a comparison between the ML techniques including Artificial Neural Networks (ANN), RF, AdaBoost and Extreme Gradient Boosting (XGBoost) suggested that the ANN outperforms the other methods for the prediction of condensation coefficient in micro-channels. [36] trained an ANN based on experimental data to predict the boiling and condensation for a refrigerant in a channel proving that the use of parameterized ANN yields accurate results. [37] employed Kalman Filter (KF) to estimate the heat flux in casting molds. The results suggested that KF offers a great performance for the estimation of heat flux in Inverse Heat Transfer Problems (IHTP). As for the applications of ML in IHTPs, [38] proposed a high-precision hybrid deep learning model based on Conventional Neural Networks (CNN) and Long Short-Term Memory (LSTM) for the time-dependent parameters. [39] predicted the radiation view factors for particles and face neighbours utilising LSTM and Gated Recurrent Unit (GRU).

Based on the studies conducted thus far, it is evident that research on impinging jets has been primarily focused on exploring various design parameters and their impact on thermal efficiency. In other words, the implementation of modern techniques, specifically ML, to mitigate the computational costs associated with the numerical simulation of impinging jets has received limited attention in this field. To address this issue, the primary objective of this study is to utilize a range of deep learning techniques, such as frequency-based MLP, LSTM, and Proper Orthogonal Decomposition (POD)-Galerkin, for predicting heat transfer. Specifically, this research aims to develop a novel deep-learning model for predicting the Nu number on a concave plate subjected to a pulsating impinging jet. Fundamentally, the prediction of Full Order Modelling (FOM) by ML methods is associated with difficulties mainly due to the presence of noise. In this regard, this study is intended to bring this issue into sharp focus. The model will consider a wide range of design parameters, including inlet velocity, frequency, and nozzle-to-surface distance as to the best of the authors’ knowledge there is yet to be any report on the prediction of the flow and geometrical parameters. In the upcoming section, this paper begins by providing a detailed problem description. Subsequently, the numerical method, encompassing the governing equation, turbulence model, geometry and grid, and validation, is presented. The subsequent sections elaborate on the deep learning models and nonlinear reduced-order models. Finally, the paper concludes with the presentation of results and discussions, followed by the conclusion.

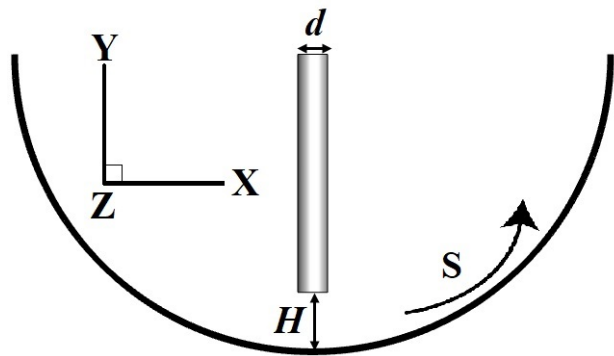


Figure 1: Schematic of the computational model

2 Full-Order Model

The numerical simulation of the heat transfer on the concave surface has been carried out with ANSYS FLUENT V2019 [40]. In the following section, the details of the full-order model are presented.

2.1 Problem Description

Fig. 1 demonstrates the schematic of the computational domain consisting of a concave surface under constant heat flux prone to a cooling jet. This model is selected based on the study of [1], where the effects of various nozzle shapes (circle, rectangle, elliptic, and square) and nozzle-to-surface distance, H/d were investigated. Given our main objective, which is the prediction of heat transfer rate on the surface, we concentrate solely on the optimal nozzle shape, i.e., the circle [1] accompanied with variable nozzle-to-surface distance. The concave surface is semi-cylindrical with a diameter of 240mm and a length of 120mm. The nozzle diameter of the circular jet was 12mm.

Additionally, we explore two different approaches for jet velocity; harmonic velocity and random inlet velocity. These approaches will be discussed in detail in the next sections.

2.2 Governing Equation

The 3-dimensional numerical simulation is carried out to investigate the effect of the geometrical and flow parameters on the heat transfer of the concave surface. In this section, the general properties of the fluid, governing equations, and solver properties will be discussed. Moreover, a further discussion on turbulence modelling will be presented.

As for the fluid properties, air with constant thermo-physical properties is considered. The fluid properties are presented in Table 1.

The governing equations of the problem including Navier-stokes and energy equations are as follows:

$$-\frac{\partial \bar{u}_i}{\partial x_i} = 0, \quad (1)$$

$$\rho \frac{\partial u_i}{\partial t} + \frac{\partial (\bar{u}_i \bar{u}_j)}{\partial x_j} = -\frac{\partial \bar{P}}{\partial x_j} + \frac{\partial}{\partial x_j} \left[\mu \left(\frac{\partial \bar{u}_i}{\partial x_j} + \frac{\partial \bar{u}_j}{\partial x_i} \right) - \rho \bar{u}_i \bar{u}_j \right], \quad (2)$$

Table 1: Thermophysical properties of the fluid

ρ	μ	k	C_p
(kg/m^3)	($Pa.s$)	(W/mK)	($J/kg.K$)
1.225	1.789e-5	0.024	1006

$$\frac{\partial \bar{T}}{\partial t} + \frac{\partial (u_i \bar{T})}{\partial x_i} = \frac{\partial}{\partial x_i} \left(\alpha \frac{\partial \bar{T}}{\partial x_i} - \overline{u_i T} \right). \quad (3)$$

2.3 Turbulence Model

Regarding equations 2 and 3, $\rho \overline{u_i u_j}$ and $\overline{u_i T}$ are the Reynolds stress tensor and turbulent heat flux, respectively. These terms can be modelled by the well-known 1- or 2-equation turbulence models as follows:

$$\overline{\rho u_i' u_j'} = \mu_\psi \left(\frac{\partial u_i'}{\partial x_j} + \frac{\partial u_j'}{\partial x_i} \right) - \frac{2}{3} \delta_{ij} \rho k, \quad (4)$$

$$\overline{\rho u_i' T'} = \frac{\mu_t}{Pr} \left(\frac{\partial T}{\partial x_j} \right), \quad (5)$$

where μ_t is turbulent viscosity, δ_{ij} is Kronecker delta and $k = u_i u_j$ is turbulent kinetic energy. To determine μ_t the $k - \omega$ turbulence model was employed which can rather precisely address the near wall phenomena. The $k - \varepsilon$ has been reported previously to outperform other turbulence models in terms of impingement jets, which will be discussed in section 2.7.

2.4 Computational Grid

A fully structured mesh has been considered for the simulation as shown in Fig. 2. To examine the independence of the numerical solution to the element size, four sets of meshes with respectively 4×10^5 , 8×10^5 , 1.5×10^6 , and 2.5×10^6 is generated. The local Nusselt number demonstrates represents the dimensionless heat transfer coefficient on a surface experiencing convective heat transfer. Fig. 3 demonstrates the variation of local Nusselt number along the concave surface (S-direction based on Fig. 1) for different grids. Clearly, the third grid corresponding to 1500000 hexahedral elements has been selected for other simulations. For all the geometries (in terms of different H/d) a fine mesh was generated near the concave surface to achieve the best accuracy of the numerical solution. It is worth noting that for capturing the near-wall physics, an element height of $10^{-6}m$ corresponding to $Y^+ < 1$ is employed for the concave surface.

2.5 Boundary and Initial Condition

The boundary conditions of the CFD model are shown in Fig. 4. The inlet temperature was set to 300K with harmonic/random velocity based on the prediction purpose. No-slip assumption along with constant heat flux was applied for the concave surface. Details of boundary conditions have been presented in Table 2. Air was modelled as incompressible flow since the Mach number is far less than 0.3

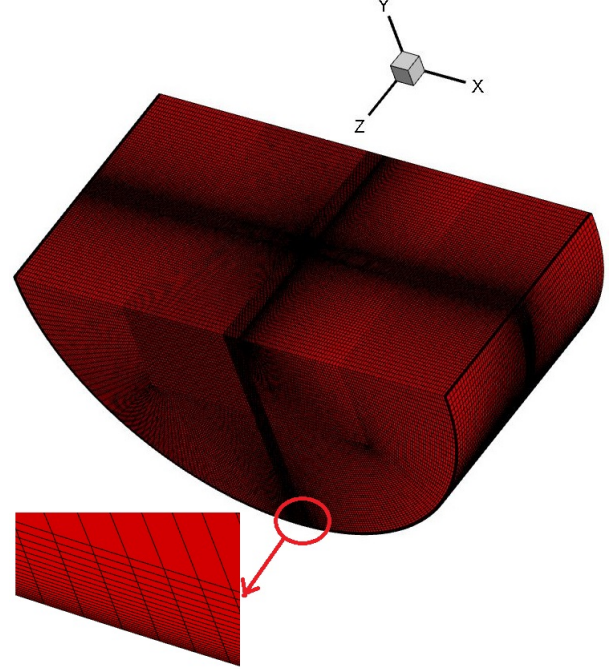


Figure 2: Structured grid for the model with a closer look at the boundary layer mesh near the concave surface

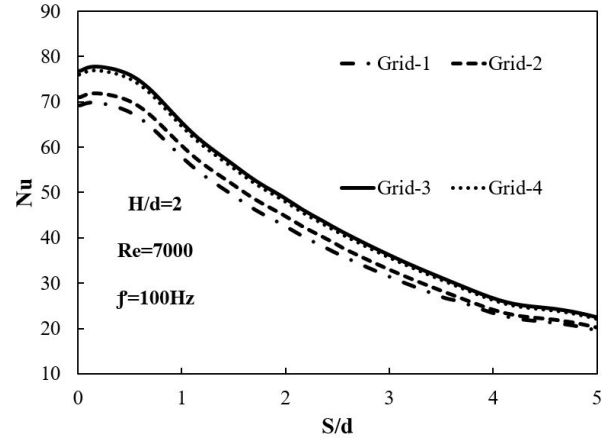


Figure 3: Variation of local Nusselt number for different meshes

Table 2: Values of the boundary conditions

Inlet	Velocity inlet: Harmonic/Random
	Inlet temperature: 300K
	Turbulence intensity: 5%
Outlet	Pressure Outlet: Gauge pressure : 0 Pa
Concave	Constant heat flux-2500W/m ²
	No-slip condition

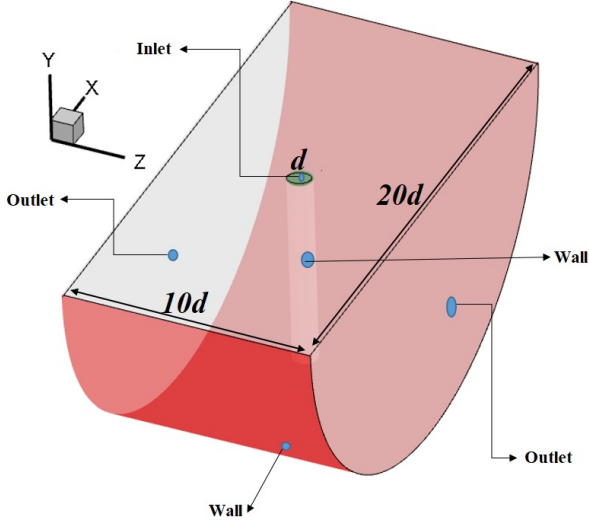


Figure 4: Utilized boundary conditions for the CFD simulation

2.6 Solver Properties

The finite volume method (FVM) was applied to discretize the governing equations. For all the equations the second-order upwind scheme was implemented to address advection terms. SIMPLE-C algorithm has been used for pressure-velocity coupling. Moreover, the time discretization has been done by the second-order implicit scheme. The timestep of the transient simulation was determined by dividing the jet pulse period by 100. To ensure the periodicity of the final solution, the simulation continued until 20 cycles. Convergence criteria were set to 10^{-4} for all equations in each time step.

2.7 Validation Study

The local Nusselt number based on the available experimental data and numerical simulation of the concave surface along the S-direction is shown in Fig. 5. A good agreement was observed between all turbulence models and the experimental data of [1]. However, they observed a comparable error for all turbulence models in the stagnation region, i.e. $S/d < 1$ and $X/d < 1$. This is due to the fact that as the jet impinges the surface, a stagnation region is generated corresponding to the values of low Reynolds numbers.

2.8 Physics of the Flow

Before exploring predictive models, we need to understand the physics of the flow in terms of impingement cooling. According to Fig. 6, the flow field of an impinging jet consists of three regions. The free jet, the impingement region and the wall jet region. These regions are highly sensitive to the effective flow and geometrical parameters including Reynolds number, nozzle-to-plate distance, nozzle section shape and surface geometry. Change in any of the mentioned parameters results in changes in the boundaries between three regions, which also subsequently affects the heat transfer from the impinging surface. Among all the

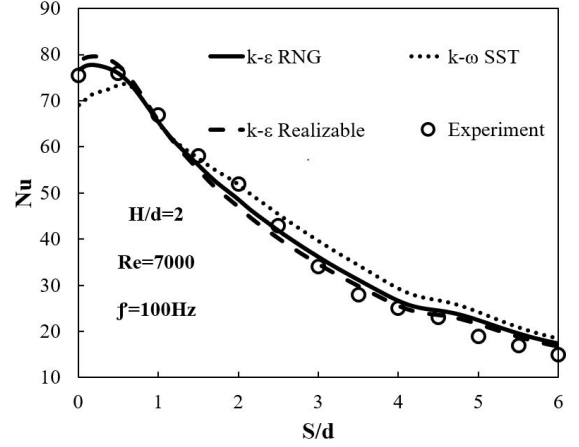


Figure 5: The performance of turbulence models to predict the local Nu number distribution

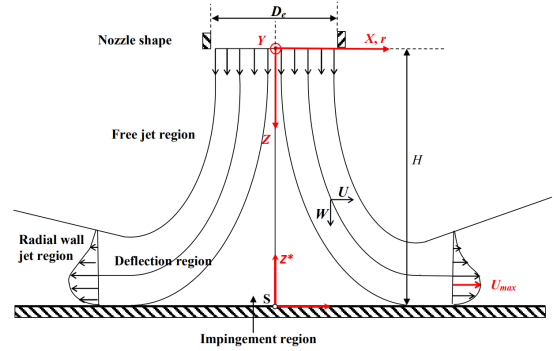


Figure 6: Formation of different regions in the context of the impinging jet on a plate [41]

available parameters, the jet velocity can be considered as the most potential variable in active flow control of the impinging jet. A change in the jet velocity and frequency causes a change in the vortex shedding frequency in the flow field, which eventually changes the formation and thickness of the boundary layer in the region of the wall jet.

Moreover, in practical cases, it is difficult to find a general correlation that can provide an explicit relationship between the heat transfer coefficient or surface temperature in terms of jet velocity. Hence, the use of advanced ML techniques such as DRL is necessary for such systems.

3 Deep Learning Models

In the following section, we explore three key architectures—Multilayer Perceptrons (MLP), Long Short-Term Memory (LSTM) and Transformers networks. These models offer unique capabilities, from MLP’s versatility in capturing non-linear relationships to LSTM’s proficiency in handling sequential data, and Transformer’s focus on long-range dependencies.

3.1 Feed-Forward Network

To generate functional relationships effectively using the deep-learning platform between the input and output, the

first simplest method is the feed-forward network, also known as multilayer perception. The schematic view of MLP is shown in Fig. 7. As shown in the figure, the input signals are denoted by the array $x = [x_1, x_2, x_3, \dots, x_N]$. As these signals are input to the neuron (shown in coloured circles), they undergo multiplication by their corresponding synaptic weights, forming the array $w = [w_1, w_2, w_3, \dots, w_N]$. This multiplication produces the value z , referred to as *activation potential*, as defined by the following formula:

$$z = \sum_{i=1}^N x_i \cdot w_i + b, \quad (6)$$

where, the additional term b , unaffected by the input array, is the bias, introducing an extra degree of freedom to the model. Subsequently, the value z undergoes transformation through an activation function *ReLU*. This function serves to constrain the value within a specific range, ultimately yielding the neuron's final output y .

3.2 Long Short Term Memory

The idea of LSTM networks was first proposed by [42] which was developed in the later studies [43]. In Fig. 8 the schematic architecture of LSTM has been presented.

One of the main advantages of LSTMs over their classic counterparts known as Recurrent Neural Networks (RNN) is their ability to recall a longer span in the time-series. More precisely, as seen in Fig. 8, an LSTM network enjoys two inputs. The input denoted by C stands for "Cell State" which is another term for the long-term memory that RNNs lack. The cell state connects all the stages of the network together going through the forget and input gates. The formulation of these gates and cell states is expressed as follows:

$$I_t = \sigma(W_{xI}x_t + W_{hI}h_{t-1} + W_{cI}c_{t-1} + B_I), \quad (7)$$

$$F_t = \sigma(W_{xF}x_t + W_{hF}h_{t-1} + W_{cF}c_{t-1} + B_F), \quad (8)$$

$$c_t = F_t c_{t-1} + I_t \tanh(W_{xc}x_t + W_{hc}h_{t-1} + B_c), \quad (9)$$

$$O_t = \sigma(W_{xO}x_t + W_{hO}h_{t-1} + W_{cO}c_t + B_O), \quad (10)$$

$$h_t = o_t \tanh(c_t), \quad (11)$$

where, $W_{xI}, W_{xF}, W_{xc}, W_{xO}$ represents matrices of weight from the input gate, forget gate, long-term cell state, output gate to input x_t , respectively. $W_{hI}, W_{hF}, W_{hc}, W_{hO}$ represents matrices of weight from the input gate, forget gate, long-term cell state, output gate to intermediate output h_{t-1} , respectively. W_{cI}, W_{cF}, W_{cO} represents matrices of weight from input gate, forget gate, output gate to cell state c_t , respectively [44]. B is the Bias vectors and $\sigma(\cdot)$ is the sigmoid function.

3.3 Transformer

The concept of Transformer models goes back to the study "Attention is all you need" introduced by [45] which revolutionized the field of Natural Language Processing (NLP). Owing to their great performance, Transformers

have been utilized in many applications including image processing techniques, denoising and machine translation. The architecture of Transformers relies heavily on the concept of "self-attention mechanisms" at the core. The self-attention mechanism enables the model to establish a relation between the relevant data points in the time series. In Fig. 9 a schematic overview of the *encoder-only* Transformer (also known as *vanilla* transformer) network has been presented.

Unlike LSTM, the Transformer has no recurrence. Instead, it utilizes the positional encoding added in the input embeddings, to maintain the sequence information. The following explanation explains the details of the transformer network.

Positional Encoding: In an encoder-only Transformer, the encoding vector for each position index t is defined as follows:

$$PE(t)_i = \begin{cases} \sin(\omega_i t), & \text{if } i \bmod 2 = 0, \\ \cos(\omega_i t), & \text{if } i \bmod 2 = 1, \end{cases} \quad (12)$$

where ω_i represents the frequency for each dimension.

Multi-head Attention: The scaled dot-product attention used by the Transformer with the Query-Key-Value (QKV) model is expressed as:

$$\text{Attention}(Q, K, V) = \text{softmax}\left(\frac{K^T}{\sqrt{D_k}}\right)V, \quad (13)$$

where queries ($Q \in \mathbb{R}^{N \times D_k}$), keys ($K \in \mathbb{R}^{M \times D_k}$), values ($V \in \mathbb{R}^{M \times D_v}$), and (N, M) denote the lengths of queries and keys (or values). D_k and D_v represent the dimensions of keys (or queries) and values, respectively. The Transformer employs multi-head attention with H different sets of learned projections instead of a single attention function.

Feed-forward and Residual Network: The feed-forward network is similar to that explained earlier. In a deeper module, a residual connection module followed by a layer normalization module is inserted around each module:

$$\begin{aligned} H_0 &= \text{LayerNorm}(\text{SelfAttn}(X) + X), \\ H &= \text{LayerNorm}(FFN(H_0) + H_0), \end{aligned} \quad (14)$$

where ($\text{SelfAttn}(\cdot)$) denotes the self-attention module, and ($\text{LayerNorm}(\cdot)$) denotes the layer normalization operation.

4 Reduced-Order Model

The POD is the most widely used technique to reduce data and extract an optimal set of orthonormal bases. In this formulation, basis functions are constructed by collecting temporal snapshots for the variable of interest during the full model solution. Each snapshot vector, $\tilde{N}u$, holds the values of the local Nu number at the center of the computational cell. The sampled values at the snapshot s are stored in the matrix $\tilde{N}\mathbf{u}_s$ with \mathcal{N} entries (\mathcal{N} being the number of nodes) to construct the snapshot matrices of $\tilde{N}\mathbf{u} = (\tilde{N}u_1, \dots, \tilde{N}u_s, \dots, \tilde{N}u_S)$. For the sake of simplicity, the details will be provided for a general snapshot matrix φ .

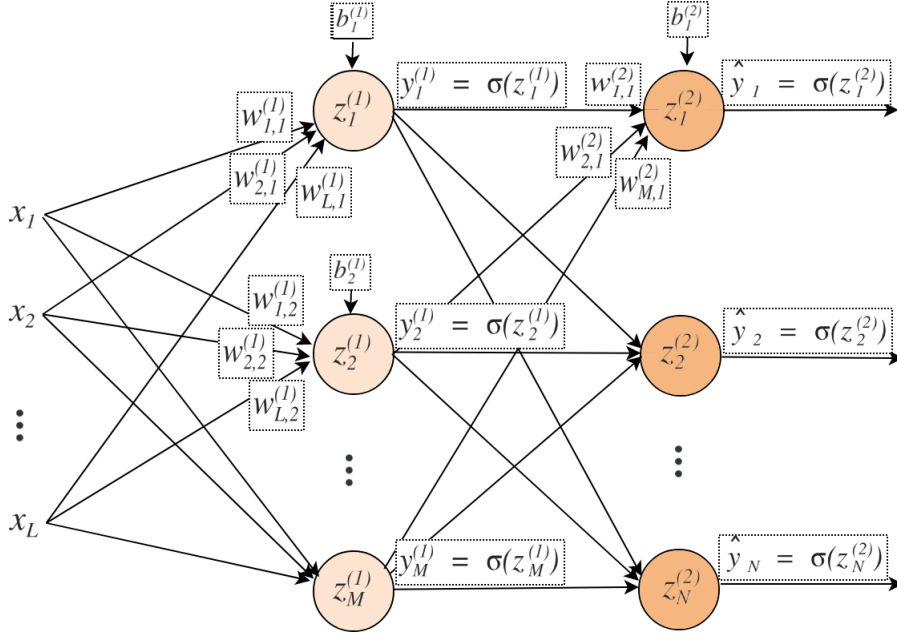


Figure 7: Structure of the feed-forward network

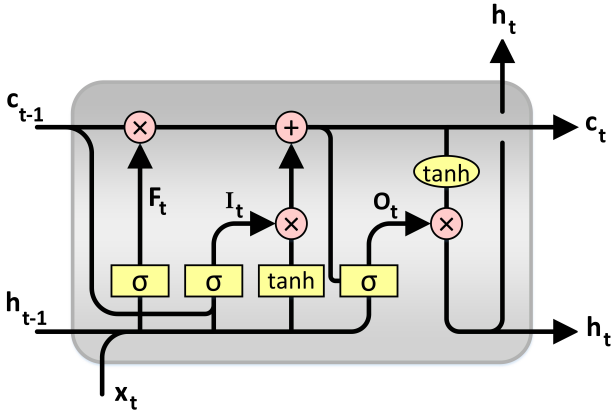


Figure 8: Structure of the LSTM block

The goal of POD is to find a set of orthogonal basis functions $\{\phi_s\}, s \in \{1, 2, \dots, S\}$, such that it maximizes:

$$\frac{1}{S} \sum_{s=1}^S |\langle \varphi, \phi_s \rangle_{L^2}|^2, \quad (15)$$

subject to:

$$\langle \phi_i, \phi_j \rangle_{L^2} = \delta_{ij} \quad (16)$$

where $\langle \cdot, \cdot \rangle_{L^2}$ is the canonical inner product in L^2 norm.

The approach introduced by [46] seeks to find an optimal set of basis functions ϕ for the optimization problem, i.e. Eq. (15). This requires performing a Singular Value Decomposition (SVD) of the snapshot matrix φ given in the form,

$$\varphi = U \Sigma V^T. \quad (17)$$

The terms $U \in \mathbb{R}^{N \times N}$ and $V \in \mathbb{R}^{S \times S}$ are the matrices that consist of the orthogonal vectors for $\varphi \varphi^T$ and $\varphi^T \varphi$,

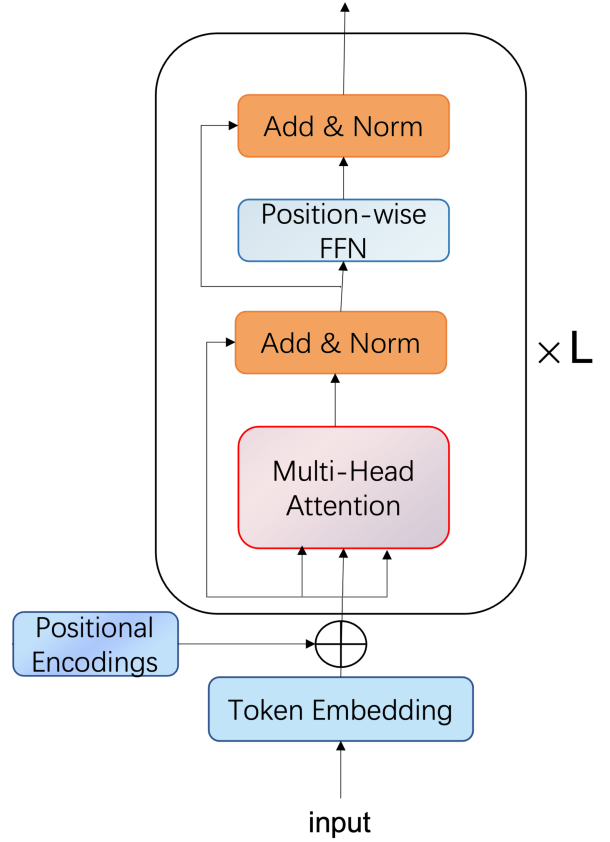


Figure 9: Structure of the encoder-only transformers network

respectively and Σ is a diagonal matrix of size $\mathcal{N} \times \mathcal{S}$. The non-zero values of Σ are the singular values of φ , and these are assumed to be listed in order of their decreasing magnitude [47]. Further on, the POD vectors can be defined as the column vectors of the matrix U . These vectors are considered to be optimal in the sense that no other rank N set of basis vectors can be closer to the snapshot matrix φ in the Frobenius norm.

A reduced-order approximation of the field can be described as follows:

$$\varphi \approx \sum_{n=1}^N \alpha_n(t) \cdot \phi_n. \quad (18)$$

The loss of information due to the truncation of the POD expansion set to N vectors can be quantified as follows:

$$L = \frac{\sum_{n=1}^N \lambda_n^2}{\sum_{n=1}^{\mathcal{S}} \lambda_n^2}, \quad (19)$$

where λ denotes singular values.

5 Results and Discussion

In this section, the results obtained by employing different model order reduction/deep learning techniques, namely MLP, LSTM, Transformer, and the combination of POD and LSTM, for the two scenarios will be investigated. These scenarios consist of a constant-frequency and a multiple-frequency impingement jet. The objective is to analyze and compare the performance of these techniques in each of the scenarios and draw meaningful conclusions from the results.

5.1 Constant-Frequency Impingement Jet

As for the simplest scenario, it was assumed that the outlet velocity of the jet oscillated with time sinusoidally with one frequency. The frequency value ranged from $5Hz$ to $100Hz$ for different cases. The average velocity, U_{jet} was also between $8m/s$ to $16m/s$ per each case. Thus, the time-dependent velocity magnitude at the inlet boundary was prescribed as follows:

$$V_{in} = U_{jet} + 0.75U_{jet} \sin(2\pi ft). \quad (20)$$

In addition to the specified flow parameters, we also considered a geometrical parameter, specifically, the ratio of the nozzle-to-jet distance to jet diameter (H/d shown in Fig. 1), which can range $2 \sim 6$. This results in a total of three independent parameters, offering a broad spectrum of variation.

To comprehensively account for the impact of changes in all variables on heat transfer performance, one needs to conduct 125 simulations by exploring five different values for each parameter. Thus, to decrease the simulation scenarios without compromising representativeness, we needed to employ a suitable design of experiment (DOE) approach. These arrays, organized tables of experimental

designs, are both efficient and balanced, enabling the simultaneous assessment of multiple factors. The method was proposed and developed by Genichi Taguchi [48–50] which is an iterative statistical method utilized for the optimization of the system whose behavior is under the influence of several parameters. In this work, the Taguchi method is employed to identify the most influential factors affecting the performance of the feed-forward neural network.

In other words, Taguchi method is mainly intended to perform an efficient sampling procedure to reduce the number of effective configurations of the parameters in the data set. In this regard, as presented in Table 3, a reduced data set has been created by Taguchi method to avoid the possible issues [51–53] related to the presence of numerous features as inputs to the MLP.

Case	H/d	Fr	V
1	2	5	8
2	2	25	16
3	2	50	14
4	2	75	12
5	2	100	10
6	3	5	10
7	3	25	8
8	3	50	16
9	3	75	14
10	3	100	12
11	4	5	12
12	4	25	10
13	4	50	8
14	4	75	16
15	4	100	14
16	5	5	14
17	5	25	12
18	5	50	10
19	5	75	8
20	5	100	16
21	6	5	16
22	6	25	14
23	6	50	12
24	6	75	10
25	6	100	8

Table 3: Cases generated for harmonic jet by Taguchi method

As outlined in Table 3, each input consist of three values: H/d , Fr , and V . The corresponding output is the Nusselt number, which varies continuously through a cycle. To adapt this continuous data for the MLP, we face the challenge of sampling it across the cycle. Due to the irregular nature of the Nusselt variations, simplifying it into a single set of data based on frequency, amplitude, and phase, similar to the input, is not feasible.

One approach is to sample the data continuously through the cycle, generating, for example, 100 discrete data points. However, maintaining a balanced dimensionality between the input and output (label) of the MLP is crucial for optimal performance. Significant differences may prevent the network from learning complex patterns

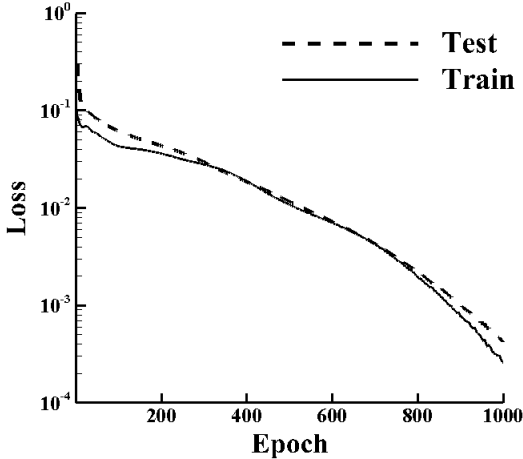


Figure 10: Train and Test loss for the MLP utilized in the constant-frequency scenario.

and hinder convergence.

To address this issue, we opted for the augmented MLP-FFT method. In this approach, the output Nusselt number is transformed into the Fourier space, providing sets of frequencies, amplitudes, and phase values. The data is organized based on amplitude, retaining only the top 10 amplitudes while discarding the others. This allows us to characterize the output Nusselt distribution using 10 sets of frequencies, amplitudes, and phases. With this transformation, we can effectively apply the MLP between the inputs and outputs. It is important to highlight that, for MLP validation, 21 out of the 25 cases were chosen for training, while the remaining four were employed for testing.

In Fig. 10 the training and test loss of the MLP has been presented. As seen below, the test loss decreases with the number of epochs approaching that of the train suggesting the successful performance of the MLP in capturing the underlying patterns and trends in the data.

The performance of the MLP with respect to the actual data has been presented in Fig. 11. From the figure, it is evident that the MLP has achieved a remarkably high level of precision in capturing the Nu number fluctuations. The close trends and values between the predicted results and the actual data demonstrate the effectiveness of the MLP in accurately modelling and reproducing the observed variations. Therefore, it is found that MLP can be regarded as an accurate tool to predict Nu number under single frequency inlet conditions. In other words, the strong agreement between the predicted values and the actual data supports the notion that the MLP can be considered as a robust and precise tool for Nu number prediction in such scenarios. This highlights the potential of MLP-based models as valuable tools in the field of fluid dynamics and heat transfer analysis.

5.2 Random-Frequency Impingement Jet

5.2.1 Average Nu Number Prediction

To take the effect of varying frequency of the impingement jet into consideration, the inlet velocity was assumed to be composed of some harmonic functions with different frequencies as follows:

$$V_{in} = \sum [U_i + 0.75U_i \sin(2\pi f_i t)], \quad (21)$$

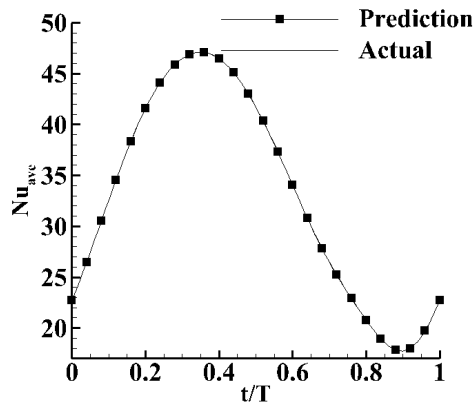
where these values were considered for the average velocity and frequency:

$$\begin{aligned} U_i &= \{8, 10, 12, 14, 16\} (m/s), \\ f_i &= \{5, 25, 50, 75, 100\} (Hz). \end{aligned} \quad (22)$$

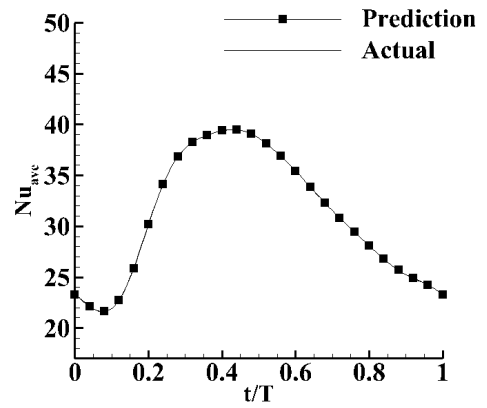
To predict the behavior of the average Nu on the plate under these conditions, two predictive networks, namely LSTM and Transformer, were employed. The objective was to draw a comparison between their respective performances in predicting the temporal variation of the average Nu on the plate. The train and test loss for both methods has been presented in Fig. 13. It should be noted that, in the case of LSTM, only the final 20 percent of the data was employed for testing, while the Transformer network, leveraging its enhanced performance attributed to the attention mechanism, was engaged for the predictions of 50 percent of the data. As is evident in Fig. 13, the test loss in both of the methods demonstrates a double descent trend. As a result, the early stopping technique was implemented to avoid poor performance [54–57]. Presented in Fig. 13 demonstrates the average Nu number predicted by the methods. It is evident in Fig. 13 that the Transformer NN has been considerably more successful in predicting the future of Nu number compared to LSTM. To illustrate, the Transformer managed to predict a longer portion of the Nu number compared to LSTM. As seen in Fig.13, almost half of the Nu number variation as a time series can be accurately predicted by the transformer, while this amount falls to less than twenty percent as seen in Fig.13a. More importantly, Transformer succeeds in predicting the amount of Nu number at each time instant with higher precision with respect to the performance of LSTM. As seen in Fig.13b, the Nu numbers predicted by Transformer fall perfectly on top of the real data obtained from the numerical simulation. However, the prediction offered by LSTM shows some discrepancies concerning the real data. Therefore, it is concluded that Transformer could be regarded as a more accurate and robust tool for predicting the Nu number on the plate subjected to a varying impingement jet compared to LSTM. This is attributed to the fact that the architecture of Transformer enjoys the attention mechanism which enables the possibility for the model to prioritize the importance of each time step in the time series. Thus, the attention mechanism leads to a more robust model owing to its capability to adapt the model to different time-dependent variability.

5.2.2 Local Nu Number Prediction

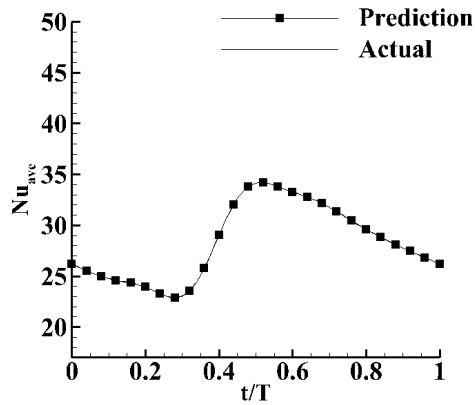
The techniques discussed so far deal with forecasting the average Nu on the plate. Despite the cardinal importance



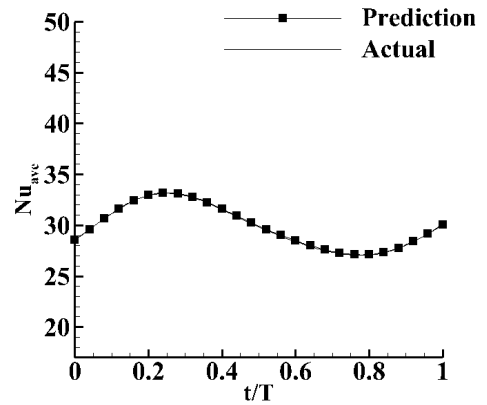
(a) case21



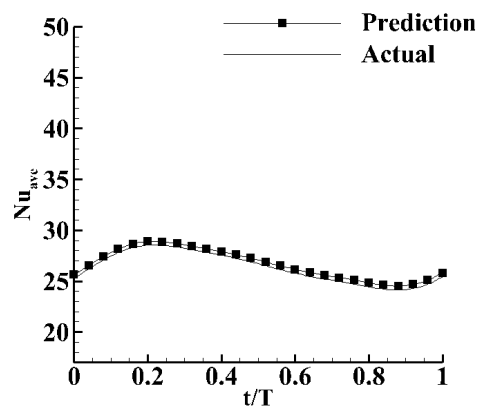
(b) case22



(c) case23

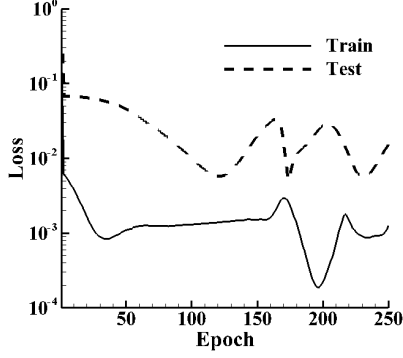


(d) case24

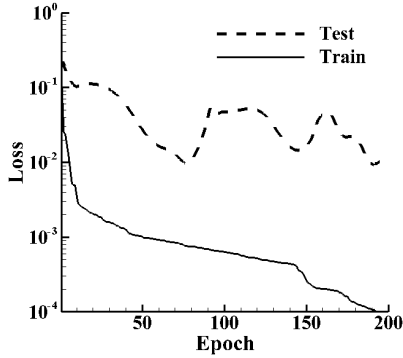


(e) case25

Figure 11: Comparison between the average Nu obtained from FOM and the MLP prediction the test cases

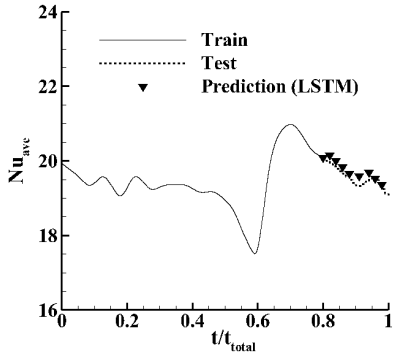


(a) Loss for LSTM

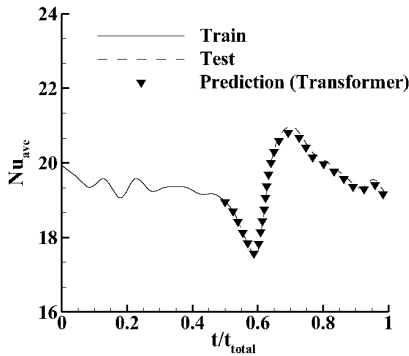


(b) Loss for Transformer

Figure 12: Comparison between the train and test loss for Transformer and LSTM



(a) LSTM



(b) Transformer

Figure 13: Comparison between the prediction made by Transformer and LSTM

of this number in engineering applications, gaining information on local Nu is crucial in many cases. In this regard, a novel method is presented in this work to work out this problem. Fundamentally, it should be noted that treating a contour as a time series is associated with some difficulties in reaching the desired accuracy especially, due to the numerous structures being present in the data structures. To address this issue, the POD+LSTM method was utilized which can be summarized in these steps, according to Fig. 15:

1. The snapshots of the variable, in this case, the Nusselt number on the symmetry boundary, have been gathered in a matrix. The POD analysis is then performed on this matrix to define the spatial orthogonal modes ϕ_n and temporal coefficients α_n . The number of modes N is selected in a way to maintain 99% of energy. Since N is much smaller than the dimension M of $\phi_n \in R^M$, the subspace expanded by ϕ_n ($n = 1, 2, \dots, N$) can be regarded as the low-dimensional representation of the full order model. α_n are then used for training in the LSTM network. It should be noted that only five modes of the snapshots matrix were considered as it corresponds to 99% of energy, as seen in Fig. 14.
2. The time series of the temporal coefficients α_n are divided into several time windows (here we take a time window of 20).
3. The time coefficients are then divided, with the initial 80% of data chosen for training, while the subsequent 20% is reserved for testing.
4. The LSTM network is trained in this part. The idea is to teach the LSTM neural network the relationship between the input and output pairs.
5. The validation of the LSTM network will be performed using the predicted time coefficients with that of the test datasets.
6. At the final step, the field will be reconstructed by using the dominant POD modes (step 1) and the predicted time coefficients obtained by the LSTM network.

In the following, the viability of this method has been evaluated. The prediction of the temporal modes corresponding to the first five dominant modes has been presented in Fig. 16 which proves the successful performance of LSTM in capturing both trend and value of each temporal modes in time. Furthermore, it is essential to analyze the accumulation of deviations between the actual and predicted values through time. Notably, the most substantial deviation is observed for the second mode, reaching a magnitude of 25% at the final time.

The impact of these deviations on the final result is completely linked to the singular values (denoted as Σ in Eq. 17) associated with each mode. For instance, referring to the cumulative Modal Energy curve in Fig. 14, the effect of deviation in the first mode (with a singular value

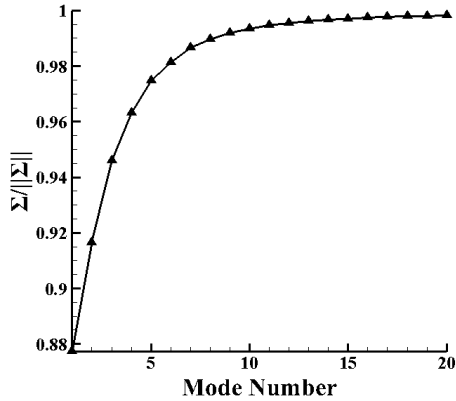


Figure 14: Cumulative Modal Energy

of approximately 0.88) can be more than 20 times that of the second mode (singular value of 0.04).

Unfortunately, the *black box* nature of predictive neural networks, including LSTM, prevents fine-tuning to prioritize one variable over another. This limitation is particularly pronounced in scenarios where the influence of certain modes needs to be prioritized, as demonstrated by the cumulative Modal Energy curve.

To visually illustrate the performance, Fig. 17 compares the contour of temperature for both the FOM and the proposed predictive surrogate model (POD-LSTM) at $t = 0.95t_{final}$. The method proposed in this work perfectly captures the physics of heat transfer on the plate at the consecutive time steps. This proves the practicality of POD for boosting the performance of time-series prediction methods especially, for local Nu on a plate subjected to an impingement jet. Additionally, the relative L2 norm error is incorporated in Fig. 17c. It reveals that the maximum error, approximately 8%, is concentrated in the region directly in front of the impingement jet. And, as one moves away from the jet, the error gradually decreases, reaching as low as 0%. This observation underscores the effectiveness of the proposed POD-LSTM model in accurately predicting temperature distribution, all over the domain.

6 Conclusion

In this paper, the heat transfer rate of a concave surface prone to an impinging jet is determined by various predictive surrogate models. The study systematically explores the impact of various model order reduction and deep learning techniques under different scenarios. For the constant-frequency impingement jet, the augmented MLP-FFT method demonstrates remarkable precision in capturing Nu number fluctuations. The study further extends to the random-frequency impingement jet, comparing the performance of LSTM and Transformer. The Transformer outperforms LSTM, showcasing its accuracy and robustness in predicting Nu numbers under varying impingement conditions. The Transformer demonstrates precise Nu number predictions for almost 50% of the cycle, whereas LSTM predictions cover only 20% of the cycle

and exhibit a higher level of error, reaching a maximum of 5%. Additionally, a novel approach combining POD and LSTM for local Nu prediction proves successful, enhancing time-series prediction for complex structures. This work underscores the potential of modern MOR and ML methods in advancing our understanding of heat transfer phenomena, which can be extended to other applications in fluid dynamics and heat transfer analysis.

References

- [1] Saeed Rakhsha, Mehran Rajabi Zargarabadi, and Seyfolah Saedodin. The effect of nozzle geometry on the flow and heat transfer of pulsed impinging jet on the concave surface. *International Journal of Thermal Sciences*, 184:107925, 2023.
- [2] M Raizner and R van Hout. Effect of impinging jet pulsation on primary and secondary vortex characteristics. *International Journal of Heat and Mass Transfer*, 151:119445, 2020.
- [3] Fatih Selimefendigil and Hakan F Öztop. Pulsating nanofluids jet impingement cooling of a heated horizontal surface. *International Journal of Heat and Mass Transfer*, 69:54–65, 2014.
- [4] Sreya Sarkar, Rohit Gupta, Tamal Roy, Ranjan Ganguly, and Constantine M Megaridis. Review of jet impingement cooling of electronic devices: Emerging role of surface engineering. *International Journal of Heat and Mass Transfer*, 206:123888, 2023.
- [5] Sunjae Kim, Jeongmin Lee, Issam Mudawar, and Jason Hartwig. Computational investigation of vertical upflow boiling of liquid nitrogen and effects of bubble collision dispersion force. *International Journal of Heat and Mass Transfer*, 203:123780, 2023.
- [6] Kiyun Kim, Pravesh Pokharel, and Taiho Yeom. Enhancing forced-convection heat transfer of a channel surface with synthetic jet impingements. *International Journal of Heat and Mass Transfer*, 190:122770, 2022.
- [7] Amirhosein Hadipour and Mehran Rajabi Zargarabadi. Heat transfer and flow characteristics of impinging jet on a concave surface at small nozzle to surface distances. *Applied Thermal Engineering*, 138:534–541, 2018.
- [8] R Van Hout, V Rinsky, and YG Grobman. Experimental study of a round jet impinging on a flat surface: flow field and vortex characteristics in the wall jet. *International Journal of Heat and Fluid Flow*, 70:41–58, 2018.
- [9] M Attalla, Ahmed A Abdel Samee, and Naser N. Salem. Experimental investigation of heat transfer of impinging jet on a roughened plate by a micro cubic shape. *Experimental Heat Transfer*, 33(3):210–225, 2020.

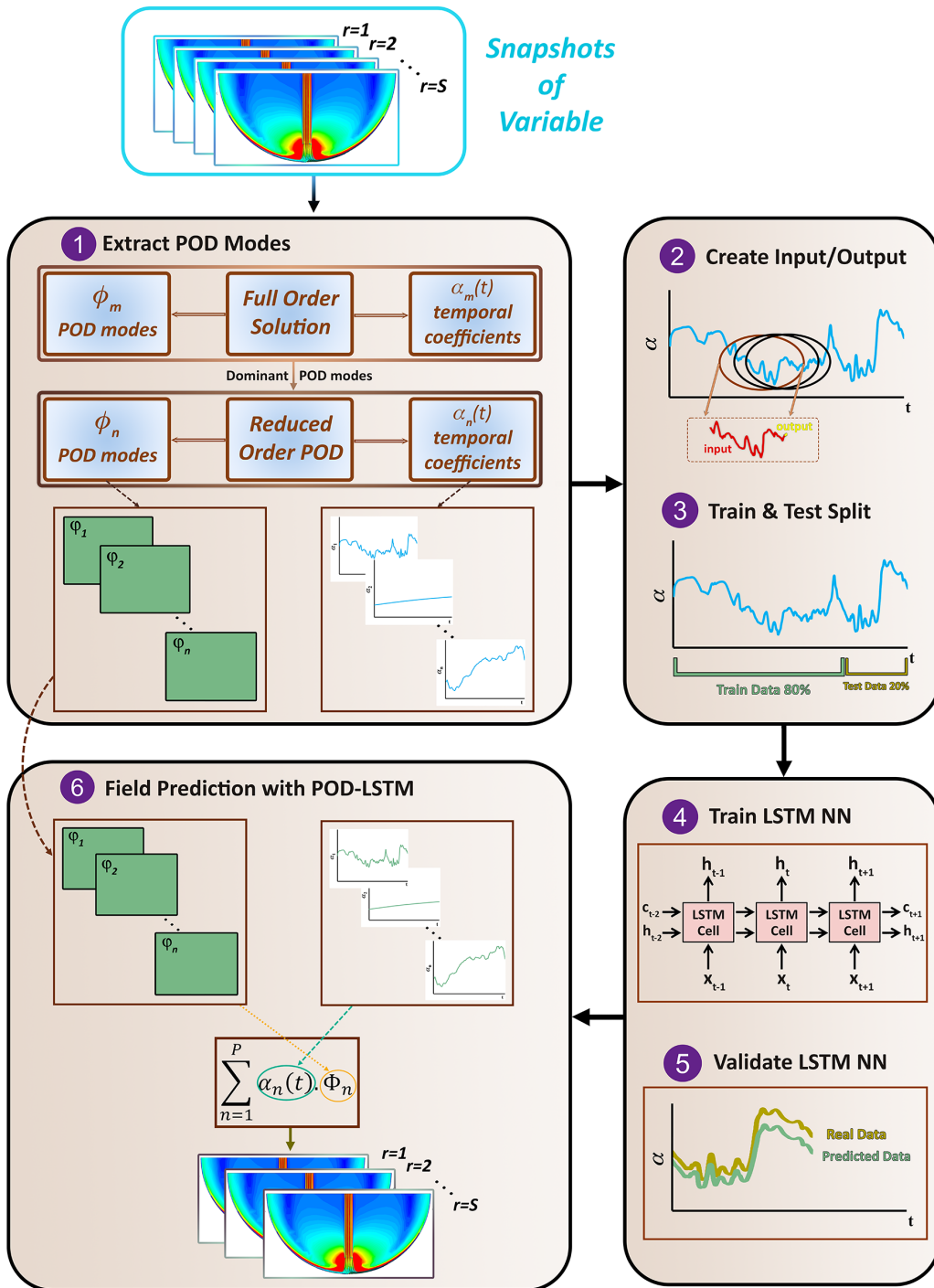
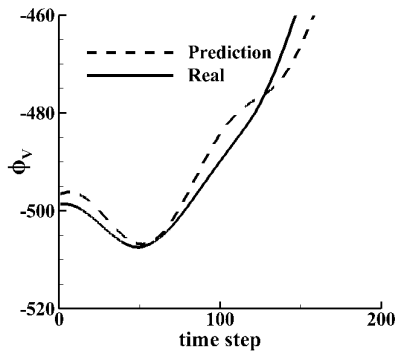
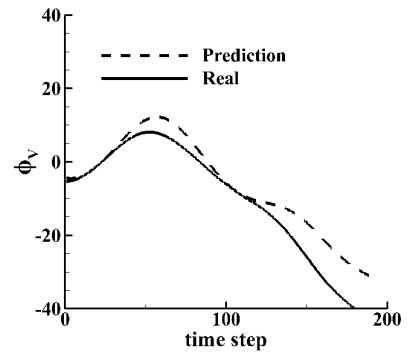


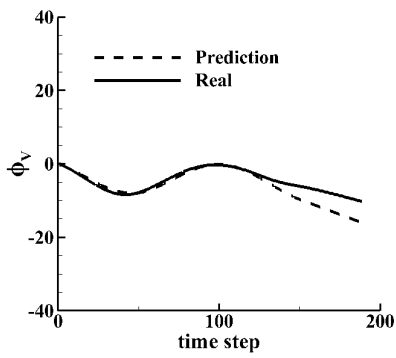
Figure 15: Structure of the POD-LSTM approach.



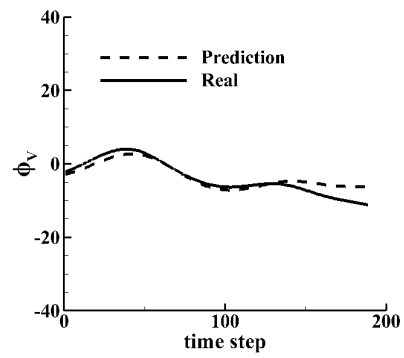
(a) Mode 1



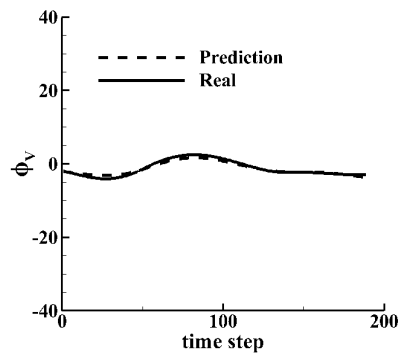
(b) Mode 2



(c) Mode 3



(d) Mode 4



(e) Mode 5

Figure 16: Comparison between actual and predicted values for different time coefficients

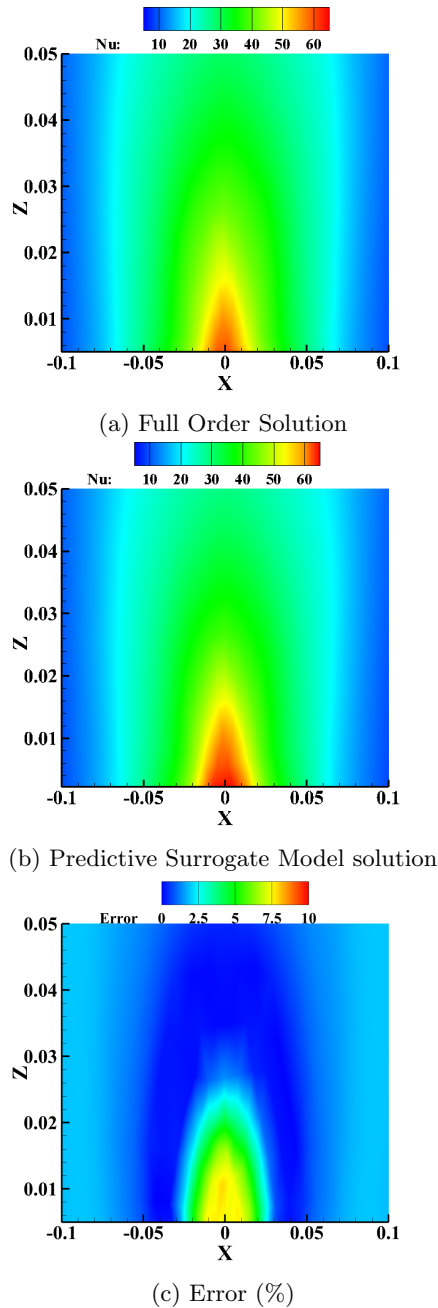


Figure 17: Comparison between full order modelling and ROM-based prediction

- [10] Muhammad Ikhlaq, Yasir M Al-Abdely, and Mehdi Khiadani. Flow and heat transfer characteristics of turbulent swirling impinging jets. *Applied Thermal Engineering*, 196:117357, 2021.
- [11] Ritesh Kumar Parida, Anil R Kadam, Madav Vasudeva, and Vijaykumar Hindasageri. Heat transfer characterisation of impinging flame jet over a wedge. *Applied Thermal Engineering*, 196:117277, 2021.
- [12] Fatih Selimefendigil and Hakan F Öztöp. Combined effects of bifurcation and magnetic field on the performance of phase change material installed cylinder with small inlet temperature perturbations during nanofluid convection. *International Journal of Heat and Mass Transfer*, 188:122640, 2022.
- [13] J Dirker, WJ Van den Bergh, HR Moran, CN Markides, and JP Meyer. Influence of inlet vapour quality perturbations on the transient response of flow-boiling heat transfer. *International Journal of Heat and Mass Transfer*, 170:121017, 2021.
- [14] Jianhui Zhao, Nan Guo, Xiangdong Lu, Jingyan Chen, Shuo Chen, and Heng Zhang. Numerical research on characteristics of fuel heating and subcooling in the nozzle hole of common rail injector. *International Journal of Heat and Mass Transfer*, 200:123508, 2023.
- [15] Anuj Kumar, Ketan Yogi, and SV Prabhu. Experimental and analytical study on local heat transfer distribution between smooth flat plate and free surface impinging jet from a circular straight pipe nozzle. *International Journal of Heat and Mass Transfer*, 207:124004, 2023.
- [16] Liang-Ching Cheng and Shwin-Chung Wong. Pore-scale numerical simulation and ltne analysis for fully-developed forced convective heat transfer in packed beds of mono-sized rough spheres covering near-wall and core regions. *International Journal of Heat and Mass Transfer*, 208:124047, 2023.
- [17] Song Li, Deyu Xu, Junming Zhao, and Linhua Liu. Random rough surface effects on the performance of near-field thermophotovoltaic system. *International Journal of Heat and Mass Transfer*, 202:123713, 2023.
- [18] Fazole Hussain and Hyder S Husain. Elliptic jets. part 1. characteristics of unexcited and excited jets. *Journal of fluid mechanics*, 208:257–320, 1989.
- [19] Hyder S Husain and Fazole Hussain. Elliptic jets. part 2. dynamics of coherent structures: pairing. *Journal of Fluid Mechanics*, 233:439–482, 1991.
- [20] Hyder S Husain and Fazole Hussain. Elliptic jets. part 3. dynamics of preferred mode coherent structure. *Journal of Fluid Mechanics*, 248:315–361, 1993.
- [21] J Mi, GJ Nathan, and RE Luxton. Centreline mixing characteristics of jets from nine differently shaped nozzles. *Experiments in Fluids*, 28(1):93–94, 2000.

- [22] Ghanshyam Singh, T Sundararajan, and KA Bhaskaran. Mixing and entrainment characteristics of circular and noncircular confined jets. *J. Fluids Eng.*, 125(5):835–842, 2003.
- [23] Sajad Alimohammadi, Darina B Murray, and Tim Persoons. On the numerical–experimental analysis and scaling of convective heat transfer to pulsating impinging jets. *International Journal of Thermal Sciences*, 98:296–311, 2015.
- [24] Jungho Lee and Sang-Joon Lee. The effect of nozzle aspect ratio on stagnation region heat transfer characteristics of elliptic impinging jet. *International journal of heat and mass transfer*, 43(4):555–575, 2000.
- [25] MF Koseoglu and S Baskaya. The role of jet inlet geometry in impinging jet heat transfer, modeling and experiments. *International Journal of Thermal Sciences*, 49(8):1417–1426, 2010.
- [26] Gerardo Paolillo, Carlo Salvatore Greco, Tommaso Astarita, and Gennaro Cardone. Effects of the swirl number, reynolds number and nozzle-to-plate distance on impingement heat transfer from swirling jets. *International Journal of Heat and Mass Transfer*, 197:123284, 2022.
- [27] Mohammed S Khan, Mohammad O Hamdan, Salah AB Al-Omari, and Emad Elnajjar. A comparison of oscillating sweeping jet and steady normal jet in cooling gas turbine leading edge: Numerical analysis. *International Journal of Heat and Mass Transfer*, 208:124041, 2023.
- [28] Shabnam Mohammadshahi, Hadi Samsam-Khayani, Tao Cai, Mahdi Nili-Ahmadabadi, and Kyung Chun Kim. Experimental study on flow characteristics and heat transfer of an oscillating jet in a cross flow. *International Journal of Heat and Mass Transfer*, 173:121208, 2021.
- [29] Xuhui Feng, Emily Cousineau, Kevin Bennion, Gilberto Moreno, Bidzina Kekelia, and Sreekant Narumanchi. Experimental and numerical study of heat transfer characteristics of single-phase free-surface fan jet impingement with automatic transmission fluid. *International Journal of Heat and Mass Transfer*, 166:120731, 2021.
- [30] Qian Xie, Yifan Wang, Xiaoqiang Li, Zhao Yang, Jiali Li, Zhihong Xie, Xianxuan Wang, Jiajia Cai, and Qiyang Xu. Two-dimensional transient heat transfer model of moving quenching jet based on machine learning. *International Journal of Heat and Mass Transfer*, 191:122765, 2022.
- [31] Minwoo Lee, Sangwoong Yoon, Juhan Kim, Yuan-gang Wang, Keeman Lee, Frank Chongwoo Park, and Chae Hoon Sohn. Classification of impinging jet flames using convolutional neural network with transfer learning. *Journal of Mechanical Science and Technology*, 36(3):1547–1556, 2022.
- [32] Elie Hachem, Hassan Ghraieb, Jonathan Viquerat, Aurélien Larcher, and P Meliga. Deep reinforcement learning for the control of conjugate heat transfer. *Journal of Computational Physics*, 436:110317, 2021.
- [33] Suvanjan Bhattacharyya, Debraj Sarkar, Rahul Roy, Shramona Chakraborty, Varun Goel, and Eydhah Al-matrafi. Application of new artificial neural network to predict heat transfer and thermal performance of a solar air-heater tube. *Sustainability*, 13(13):7477, 2021.
- [34] Javad Mohammadpour, Shahid Husain, Fatemeh Salehi, and Ann Lee. Machine learning regression-cfd models for the nanofluid heat transfer of a microchannel heat sink with double synthetic jets. *International Communications in Heat and Mass Transfer*, 130:105808, 2022.
- [35] Liwei Zhou, Deepak Garg, Yue Qiu, Sung-Min Kim, Issam Mudawar, and Chirag R Kharangate. Machine learning algorithms to predict flow condensation heat transfer coefficient in mini/micro-channel utilizing universal data. *International Journal of Heat and Mass Transfer*, 162:120351, 2020.
- [36] Guangya Zhu, Tao Wen, and Dalin Zhang. Machine learning based approach for the prediction of flow boiling/condensation heat transfer performance in mini channels with serrated fins. *International Journal of Heat and Mass Transfer*, 166:120783, 2021.
- [37] Yukimi Oka and Munekazu Ohno. Parameter estimation for heat transfer analysis during casting processes based on ensemble kalman filter. *International journal of heat and mass transfer*, 149:119232, 2020.
- [38] Feiding Zhu, Jincheng Chen, Yuge Han, and Dengfeng Ren. A deep learning method for estimating thermal boundary condition parameters in transient inverse heat transfer problem. *International Journal of Heat and Mass Transfer*, 194:123089, 2022.
- [39] A Kianimoqadam and J Lapp. Calculating the view factor of randomly dispersed multi-sized particles using hybrid gru-lstm recurrent neural networks regression. *International Journal of Heat and Mass Transfer*, 202:123756, 2023.
- [40] Inc. ANSYS. Ansys fluent user’s guide, version 2019 r3, 2019.
- [41] Kodjovi Sodjavi, Brice Montagné, Pierre Bragança, Amina Meslem, Florin Bode, and Magdalena Kristiawan. Impinging cross-shaped submerged jet on a flat plate: a comparison of plane and hemispherical orifice nozzles. *Meccanica*, 50:2927–2947, 2015.
- [42] Sepp Hochreiter and Jürgen Schmidhuber. Long short-term memory. *Neural computation*, 9(8):1735–1780, 1997.
- [43] Greg Van Houdt, Carlos Mosquera, and Gonzalo Nápoles. A review on the long short-term memory model. *Artificial Intelligence Review*, 53:5929–5955, 2020.

- [44] Evangelin Dasan and Ithayarani Panneerselvam. A novel dimensionality reduction approach for ecg signal via convolutional denoising autoencoder with lstm. *Biomedical Signal Processing and Control*, 63:102225, 2021.
- [45] Ashish Vaswani, Noam Shazeer, Niki Parmar, Jakob Uszkoreit, Llion Jones, Aidan N Gomez, Łukasz Kaiser, and Illia Polosukhin. Attention is all you need. *Advances in neural information processing systems*, 30, 2017.
- [46] Lawrence Sirovich. Turbulence and the dynamics of coherent structures. i. coherent structures. *Quarterly of applied mathematics*, 45(3):561–571, 1987.
- [47] D Xiao, F Fang, CC Pain, IM Navon, P Salinas, and A Muggeridge. Non-intrusive reduced order modeling of multi-phase flow in porous media using the pod-rbf method. *J Comput Phys*, 1:1–25, 2015.
- [48] Genichi Taguchi and Madhav S Phadke. Quality engineering through design optimization. In *Quality control, robust design, and the Taguchi method*, pages 77–96. Springer, 1989.
- [49] Genichi Taguchi. Quality engineering (taguchi methods) for the development of electronic circuit technology. *IEEE transactions on reliability*, 44(2):225–229, 1995.
- [50] Genichi Taguchi and Rajesh Jugulum. *The Mahalanobis-Taguchi strategy: A pattern technology system*. John Wiley & Sons, 2002.
- [51] Dinesh Singh, Héctor Climente-González, Mathis Petrovich, Eiryo Kawakami, and Makoto Yamada. Fsnets: Feature selection network on high-dimensional biological data. In *2023 International Joint Conference on Neural Networks (IJCNN)*, pages 1–9. IEEE, 2023.
- [52] Anamika Dhillon and Gyanendra K Verma. Convolutional neural network: a review of models, methodologies and applications to object detection. *Progress in Artificial Intelligence*, 9(2):85–112, 2020.
- [53] Yanrui Jin, Zhiyuan Li, Chengjin Qin, Jinlei Liu, Yunqing Liu, Liqun Zhao, and Chengliang Liu. A novel attentional deep neural network-based assessment method for ecg quality. *Biomedical Signal Processing and Control*, 79:104064, 2023.
- [54] Preetum Nakkiran, Gal Kaplun, Yamini Bansal, Tristan Yang, Boaz Barak, and Ilya Sutskever. Deep double descent: Where bigger models and more data hurt. *Journal of Statistical Mechanics: Theory and Experiment*, 2021(12):124003, 2021.
- [55] Mikhail Belkin, Daniel Hsu, and Ji Xu. Two models of double descent for weak features. *SIAM Journal on Mathematics of Data Science*, 2(4):1167–1180, 2020.
- [56] Marco Loog, Tom Viering, Alexander Mey, Jesse H Krijthe, and David MJ Tax. A brief prehistory of double descent. *Proceedings of the National Academy of Sciences*, 117(20):10625–10626, 2020.
- [57] Juntao Fei and Cheng Lu. Adaptive sliding mode control of dynamic systems using double loop recurrent neural network structure. *IEEE transactions on neural networks and learning systems*, 29(4):1275–1286, 2017.